Version of Record: https://www.sciencedirect.com/science/article/pii/S092583882300871X
Manuscript_97675d4a0174378e77ca0b87b7ba938e

Gas Nitriding Behavior of Refractory Metals and Implications for Multi-Principal Element Alloy Design

Yu-Hsuan Lin[a], Andre Bohn[a], Justin Y. Cheng[a], Anette von der Handt[b], Nathan A. Mara[a], David L. Poerschke[a,1]

[a] *Department of Chemical Engineering and Materials Science, University of Minnesota, Minneapolis, MN 55455, USA*

[b] *Department of Earth Sciences, University of Minnesota, Minneapolis, MN 55455, USA*

Multi-principal element alloys (MPEAs) comprise a large, flexible compositional space that enables tuning of their chemistry, structure, and properties. To facilitate the development of nitriding-based surface-enhancement strategies that harness a broad compositional space, this study examined the gas nitriding behavior of Hf, Mo, Nb, Ta, Ti, and Zr as a function of time, temperature (750 and 1000 ºC), and nitriding potential (i.e. ammonia-to-hydrogen ratio). These metals were selected because they have a strong driving force to form nitrides, and appear in many promising refractory MPEA compositions. The nitriding temperatures were selected based on the phase transformation temperature of Ti and Zr, and the nitriding potentials were chosen such that all elements are expected to form nitrides. Mass gain measurements indicate that all six elements follow parabolic kinetics. The microstructure observations and quantitative microchemical analysis show formation of dense and well-adhered compound layers for Mo, Nb, and Ta. Thick diffusion zones appear in Hf, Ta, Ti, and Zr, and diffusion coefficients were fit to the composition profiles. Partial delamination of the compound layer occurred for Ti and Zr. Peak hardness values above 30 GPa are obtained in the dense compound layers, and the solute hardening of the underlying alloy is correlated with the nitrogen content. The results provide insight into the dynamics of nitride compound formation relative to interstitial dissolution of nitrogen, and are discussed in the context of MPEA composition and processing design.

Keywords: Nitride Materials, Diffusion, Mechanical Properties, Refractory Metals, Gas-Solid Reactions

[1] Corresponding author: dpoersch@umn.edu +1-612-625-7874

1 INTRODUCTION

Materials exhibiting combinations of high temperature strength, high toughness, and wear and corrosion resistance are needed to increase the performance, efficiency, and component life for a variety of transportation and energy conversion systems. Over the past decade, research has shown that multi-principal element alloys (MPEAs) offer promising properties for these advanced engineering applications [1–6]. Different from conventional alloys with a single base element, MPEAs are defined to contain at least 5 principal metallic elements with the concentration of each element between 5 to 35%. A combination of favorable mixing enthalpy and high configurational entropy allows these alloys to form ductile, high symmetry solid solution phases, rather than more brittle intermetallic phases. This expands the compositional flexibility to simultaneously tune the mechanical properties and aspects of the alloy chemistry related to processibility and corrosion resistance. Many families of MPEAs have been studied; the most mature systems are based on either primarily 3d transition metals, or refractory metals [7]. The 3d transition metal MPEAs show superior yield strength compared to conventional alloys at lower temperatures, and the refractory MPEAs retain high yield strength to even higher temperatures [8].

Surface enhancement processes are regularly used to modify the surface properties relative to the bulk properties. Nitriding is one common method to increase the surface hardness to improve the wear, fatigue, and corrosion resistance while maintaining a tough, ductile core. In this process, the component is exposed to a reactive, high nitrogen activity atmosphere leading to nitrogen dissolution into the alloy and the formation of nitride compounds on the surface. In conventional alloys, the surface nitride compound layer is often limited to nitrides of the major alloy component, which may not offer desirable properties. For example, tool steels can form undesirable iron nitrides at the surface by gas nitriding. Therefore, steel components are commonly coated with TiN by physical vapor deposition to take advantage of the higher hardness, lower wear rate and better oxidation resistance offered by TiN [9]. However, the coating process adds to the manufacturing cost without improving the base metal properties. Conversely, because MPEAs have significant fractions of multiple elements, it could be possible for them to form multi-component nitrides or solid solution nitrides known to have better properties than binary nitrides [10–12].

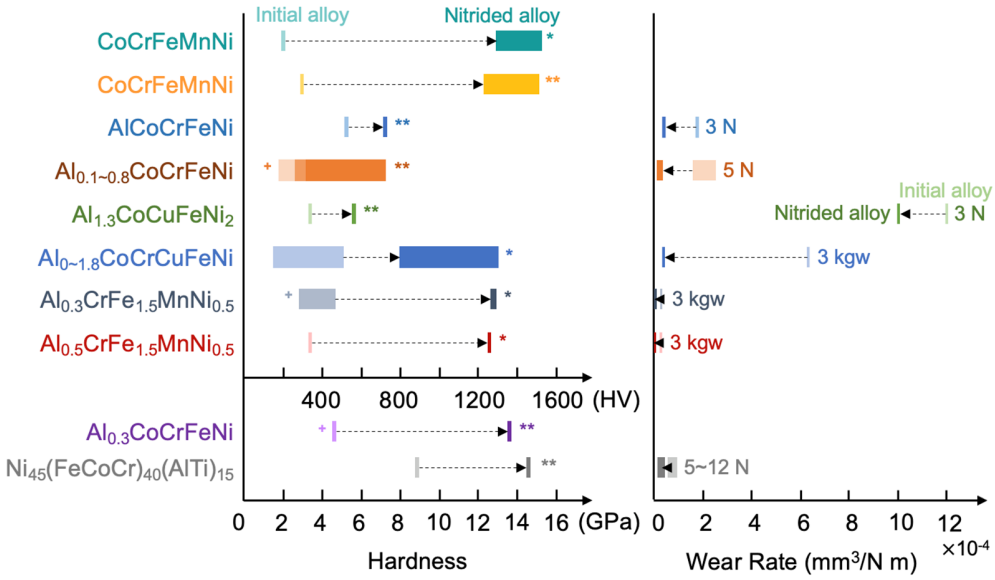

Figure 1. Reported surface hardness increases and wear rate reductions for nitrided transition metal MPEAs including CoCrFeMnNi [13], CoCrFeMnNi [14], AlCoCrFeNi [15], $Al_xCoCrFeNi$ [16], $Al_{1.3}CoCuFeNi_2$ [17], $Al_xCoCrCuFeNi$ [18], $Al_{0.3}CrFe_{1.5}MnNi_{0.5}$ [19], $Al_{0.5}CrFe_{1.5}MnNi_{0.5}$ [20], $Al_{0.4}CoCrFeNi$ [21], $Ni_{45}(FeCoCr)_{40}(AlTi)_{15}$ [22]. The arrows indicate the direction of property change from the initial alloy to after nitriding, the width of the color bars represents the range of values reported, * represents peak hardness, and ** represents hardness measured from the surface. Alloys were in the as-cast or -received state unless marked with '+', which indicates the alloy had been annealed first.

Initial reports based on adding nitride-forming Al, Cr, or Ti to 3d transition metal MPEAs suggest that nitriding can be successfully applied to further enhance the properties of these alloys [13–22]. **Figure 1** shows the hardness and wear rate change of several MPEAs after nitriding. In those studies, the surface hardness of the nitrided material was increased by up to a factor of four, and the wear resistance increased by up to two orders of magnitude. Likewise, there has been research into the properties of MPEA-based nitride coatings deposited by sputtering and related techniques. These generally show excellent hardness and wear resistance. For example, sputtered (TiZrNbHfTa)N [10], (TiZrHfVNb)N [23,24], and (TiZrTaVNbHf)N [25] coatings were all shown to be FCC solid solution nitrides with hardness values up to 30~60 GPa. Exciting opportunities exist to design alloys that could form these complex nitrides via a direct nitriding process, while also maintaining favorable bulk properties.

Despite these promising results, nitriding processes have been studied for relatively few MPEAs, and mostly those with a small fraction of the nitride forming elements. To harness the full potential of the compositional flexibility afforded by MPEAs, it is important to explore other

alloy systems based either on adding additional nitride-forming elements to 3d transition metal MPEAs, or by designing alloys based primarily on nitride-forming refractory metals. In addition, refractory MPEAs are found to have superior properties for high-temperature load-bearing structures are needed [1,8]. Nitrided surfaces and nitride coatings based on refractory alloys have good thermal stability, very high hardness, and tribological properties like low friction and wear resistance [9–11,25–29]. Therefore, nitriding would be a promising way to further improve the endurance life of components composed of refractory-metal based MPEAs.

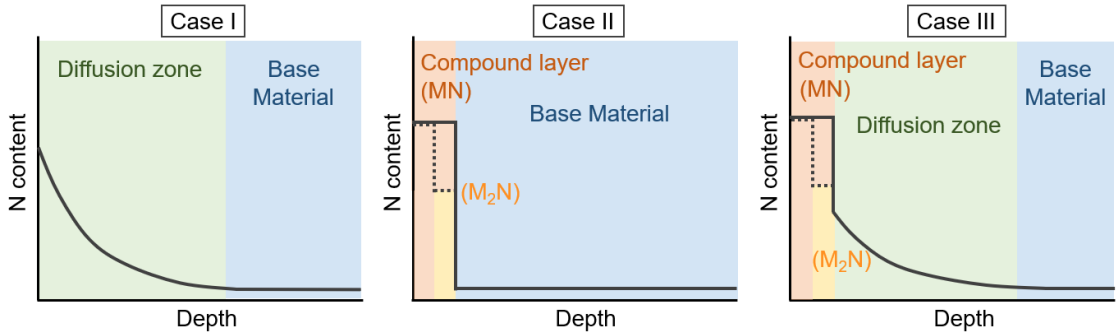

Figure 2. Depending on the alloy characteristics, nitriding can lead to one of three distinct surface microstructures and nitrogen concentration profiles. Formation of a diffusion zone, a compound layer, or both are the three possible cases. In cases where compound layers are present, the formation of layers of different compound stoichiometries (e.g., MN, M_2N, etc.) is possible.

During the nitriding process, the surface reaction pathway (**Figure 2)** is controlled by alloy characteristics including the nitrogen solubility and nitrogen diffusivity in the alloy, and the thermodynamic stability of constituent metal nitride compounds. In Case I shown in **Figure 2,** interstitial dissolution and diffusion into the base alloy produce a moderately hardened diffusion zone. Alternatively, a layer comprising one or more very hard nitride compounds can form at the surface (Case II), or the two processes can happen concurrently (Case III). The compound layer is responsible for tribological and corrosion behaviors [30], and the graded structure can prevent early spallation observed when hard nitrides are deposited directly onto softer alloys, i.e. the eggshell effect, and contributes to fatigue endurance [30]. For alloys with high interstitial nitrogen solubility, low nitride stability, or fast interstitial nitrogen diffusion, the nitrogen activity at the surface may never be sufficient to form a nitride compound layer. Conversely, for alloys with low nitrogen solubility or nitrogen diffusivity, the compound layer develops without a subsurface diffusion zone. It is expected that the nitride stoichiometry and structure for MPEAs can be controlled by tuning the alloy chemistry. However, given the large compositional space

for MPEAs, it is important to first understand the nitriding behavior of individual elements to efficiently narrow and navigate the design space.

Table 1. Solubility limits and possible nitride phases (based on [31–38]), and calculated volume expansion ratios (VERs) of Hf, Mo, Nb, Ta, Ti, and Zr.

Metal	**Solubility limit (at%)**		**Other Nitrides**	**M_2N**	**MN**
	750 ºC	**1000 ºC**			
Hf	28	28	Hf_3N_2 ($R\bar{3}m$) [VER: 1.03]	-	$Fm\bar{3}m$ [VER: 1.04]
Mo	0	0	-	β ($I4_1/amd$) [VER: 1.15] γ ($Fm\bar{3}m$) [VER: 1.16]	δ ($P6_3mc$) [VER: 1.28]
Nb	0	1	γ-Nb_4N_3 ($I4/mmm$) [VER: 1.15]	β ($P6_3/mmc$) [VER:1.11]	ε ($P6_3/mmc$) [VER: 1.18] δ ($Fm\bar{3}m$) [VER: 1.16]
Ta	3	5	-	γ ($P6_3/mmc$) [VER: 1.11]	ε ($P6/mmm$) [VER: 1.31]
Ti	14	23	-	$P4_2/mnm$ [VER: 1.08]	$Fm\bar{3}m$ [VER: 1.08]
Zr	22	23	-	-	δ ($Fm\bar{3}m$) [VER: 1.06]

To help develop this understanding, we investigated the gas (NH_3 + H_2) nitriding behavior of hafnium (Hf), molybdenum (Mo), niobium (Nb), tantalum (Ta), titanium (Ti), and zirconium (Zr). These refractory metals form stable nitrides and their high melting temperatures could enable alloys for high temperature applications. The possible nitride phases and interstitial nitrogen solubility limits at the nitriding temperatures selected for this work were determined from the relevant phase diagrams [31–38] in **Figure 3** and are listed in **Table 1**. The two nitriding temperatures, 750 ºC and 1000 ºC, were selected to capture behavior above and below the phase transformation temperatures of pure Ti and Zr, which are 883 ºC and 862 ºC, respectively. The increase in the molar volume upon forming each nitride (volume expansion ratio, VER), which is akin to the Pilling-Bedworth ratio used to characterize thermally grown

oxides, was calculated for each nitride based on the densities of the phases [39–42]; these results are also tabulated in **Table 1**. The small increase in volume when forming most nitrides limits growth stresses. Below 1000 ºC, each element except Zr has a subnitride phase in the form of M_2N or M_4N_3 (M = Metal). All except Mo can form MN nitrides with the rock salt structure, which are among some of the hardest known phases. However, the rock salt MN stability range is limited for some elements, and δ-MoN, ε-NbN, and ε-TaN have hexagonal structures for the temperatures studied herein. The high N solubility limits for Hf, Ti, and Zr should facilitate forming diffusion zones. Gas nitriding using ammonia as a high-activity nitrogen source and hydrogen as a moderating gas enables precise control of the chemical environment, with few limitations on geometry [43,44] while using simple equipment [45]. The nitriding potential (r_N) is determined by the partial pressures of ammonia (p_{NH_3}) and hydrogen (p_{H_2}) [46]:

$$r_N = \frac{p_{NH_3}}{p_{H_2}^{\frac{3}{2}}} \tag{1}$$

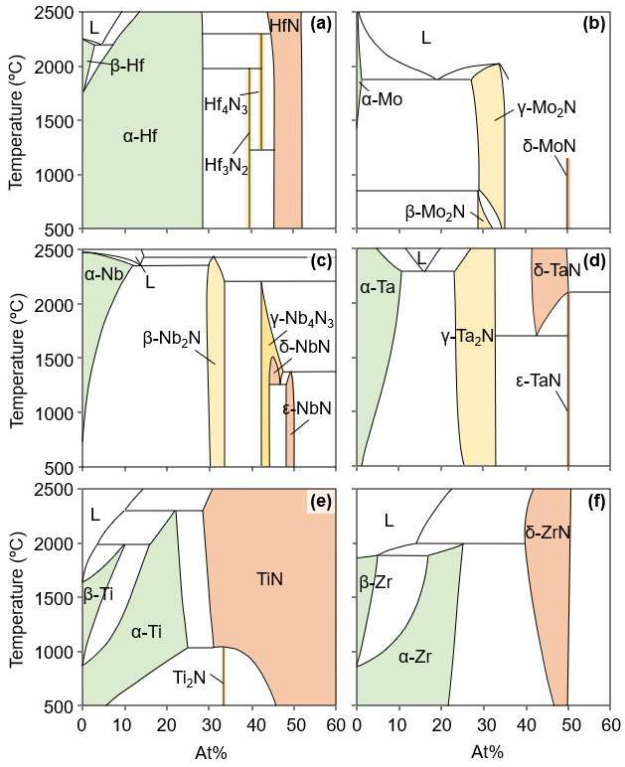

Figure 3. Schematic binary phase diagrams illustrating stables phases and solid solution ranges for (a) Hf-N [31,32], (b) Mo-N [33], (c) Nb-N [32,34], (d) Ta-N [35,36], (e) Ti-N [37], and (f) Zr-N [32,38]**.**

In this work, nitriding potentials of 3.46 and 1825 $atm^{-1/2}$ were selected. These are relatively high compared to the nitriding potentials required to form the nitrides, meaning that the nitrides should be thermodynamically stable. The range of three orders of magnitude allows comparison of the influence of the nitriding potential on kinetic effects.

Prior studies of the gas nitriding of these elements, as elaborated in the following summary, provides initial insight into the dynamics of compound layer and diffusion zone formation. However, this prior work used a wide variety of process conditions, and impurities (e.g., oxygen) were present in some cases. These factors make it difficult to distinguish differences in the intrinsic nitride growth dynamics from differences in the processing conditions. Russell et al. [47] nitrided Hf at 876-1034 ºC using various pressures of N_2, and found that HfN formed after nitriding and the weight of N uptake per unit area follows parabolic kinetics. Lengauer et al. [48] also nitrided Hf in N_2, but at much higher temperatures: at 1340 ºC, δ-HfN_{1-x}, ζ-Hf_4N_{3-x}, and η-Hf_3N_{2-x} formed, but only δ-HfN_{1-x} and ζ-Hf_4N_{3-x} appeared at 1700 ºC. Nagae et al. [49] nitrided Mo at 1100 ºC using flowing NH_3, producing γ-Mo_2N and β-Mo_2N outer and inner layers. Martinz et al. [50] reported that Mo nitrided in flowing NH_3 in the range 800 ºC to 1200 ºC only formed γ-Mo_2N (not β-Mo_2N) with roughly parabolic kinetics. Ufuktepe et al. [51] used N_2 to do short-time nitriding (5-80 min) on Nb at 900 ºC producing β-Nb_2N (hardness ~ 26 GPa) with thickness following a parabolic law. Lengauer et al. [52] annealed Nb in N_2 at 1100-1400 ºC, and found that β-Nb_2N, γ-$Nb_4N_{3\pm x}$, and η-NbN formed below 1300 ºC; above 1320 ºC the η-NbN transforms to δ-NbN_{1-x}. Prokoshkin et al. [53] nitrided Ta in N_2, and report parabolic kinetics with hexagonal Ta_2N and γ'-MoC-type TaN at 600-850 ºC, and WC-type TaN rather than γ'-TaN at 900-1000 ºC. Ajikumar et al. [54] nitrided Ti in a mixture of NH_3 and Ar at 1000 ºC, and obtained Ti_2N and TiN with a peak harness of 2000 kg/mm^2 at the surface and a gradual decrease towards the base material. Yoshida et al. [55] also observed Ti_2N and TiN using N_2 at 800 ºC. Reger et al. [56] annealed Zr in flowing N_2 at 600 ºC and 800 ºC, and observed Zr_2N, ZrN, ZrO_2, $Zr_7O_8N_4$ with an increase of hardness from 252 HV to 492-1365 HV.

The nitriding process is controlled by a complex interplay of the surface reactions liberating nitrogen from NH_3, the nitrogen dissolution and diffusion kinetics, as well as the thermodynamics controlling interstitial solubility and compound formation. To serve as a reference for the design of MPEAs used for nitriding, e.g., to enable precise control over the nitride structures and the relative thickness of the nitride compound layer and diffusion zone in

MPEAs, it is crucial to understand these dynamics under equivalent conditions. To address this need, this work compares the gas nitriding behavior of six pure refractory metals as a function of time, temperature, and nitriding potential. Mass gain measurements were used to quantify nitridation kinetics, and microstructure characterization and nanoindentation mapping were used to connect chemistry, structure, and mechanical properties. The comprehensive information obtained provides a foundation for future studies exploring the MPEA design space.

2 EXPERIMENTAL METHODS

2.1 Materials and Nitriding Procedure

Hafnium (Hf, 99.7% pure excluding Zr), molybdenum (Mo, 99.4%), niobium (Nb, 99.8%), tantalum (Ta, 99.95%), titanium (Ti, 99.7%), and zirconium (Zr, 99.2% pure excluding Hf) wires between 1 mm and 2 mm diameter were procured from Alfa Aesar (all purities given on a metals basis). Specimens approximately 20 mm long were cut from the wires, and their surfaces were polished with diamond suspensions (to 1 μm) and then ultrasonically cleaned using micro-organic soap. The specimens were held within a quartz furnace tube using a quartz holder that supports the specimen ends orthogonal to the flow direction. This configuration exposed the sample uniformly to the reactive gas while limiting interruption of the gas flow.

Nitriding was performed in a constant flowing gas mixture containing ammonia (NH_3 99.99% purity, Matheson) and hydrogen (H_2 99.999% purity, Matheson). The relative proportion of these gases determines the nitriding potential. The individual gas flows were controlled by mass flow controllers (Alicat, MCS-Series for NH_3 and MC-Series for H_2) to vary the nitriding potential while maintaining a total flow rate (q) of 150 sccm. For each experiment, the tube was flushed with the process gas, then the samples were heated at 20 ºC/min, held for the prescribed dwell, and cooled at 10 ºC/min in the process gas. The test matrix considered combinations of nitriding potential (r_N = 3.46 $atm^{-1/2}$, achieved with q_{H2} = 50 sccm and q_{NH3} = 100 sccm, or 1825 $atm^{-1/2}$, achieved with q_{H2} = 1 sccm and q_{NH3} = 149 sccm), temperature (750 ºC or 1000 ºC) and time (1 h, 5 h, and 20 h dwell). Experiments were also performed without a dwell (0 h) to establish a baseline accounting for reactions during the heating and cooling transients. All conditions were tested at 1000 ºC; based on the initial results only the longer times (5 h and 20 h) and higher r_N (1825 $atm^{-1/2}$) were tested at 750 ºC. The selected nitriding potentials are well above the minimum nitriding potential to stabilize each stoichiometric nitride (**Figure 4)**. At the same time,

the approximately three orders of magnitude difference between the selected conditions is still expected to reveal relevant differences in the relative dynamics of surface dissolution, diffusion into the alloy, and nucleation of the nitrides.

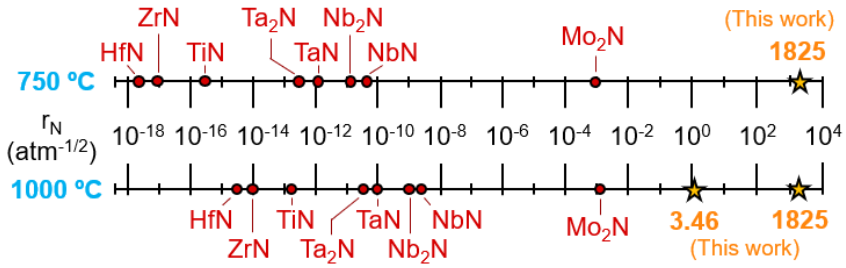

Figure 4. The minimum nitriding potential required to form each stoichiometric metal nitride at 750 ºC and 1000 ºC. The experimental conditions (r_N = 3.46 and 1825 $atm^{-1/2}$) are shown for comparison. (Calculated using thermodynamic data from the FactSage FactPS database [59].)

2.2 Characterization

The samples were weighed before and after nitriding using a balance with readability of 0.01 mg. Changes in color and sheen, and evidence of cracking were noted. The samples were then cross sectioned, mounted in epoxy, and polished to a 1 µm finish with diamond suspensions. Some of the samples were then vibratory polished using 0.03 µm colloidal silica for crystallographic analysis and hardness measurements. The cross-section microstructures were observed using backscattered scanning electron microscopy (BS-SEM, Hitachi SU8230) operated at 10 kV. Crystal structures of the nitrided phases were identified using electron backscatter diffraction (EBSD, JEOL 6500 FEG-SEM equipped with Oxford Instruments Symmetry EBSD detector) with a 20 kV accelerating voltage and a 0.1 µm step size. The compositions of the nitrided regions were measured by electron probe microanalysis with wavelength dispersive spectroscopy (EPMA, WDS, JEOL JXA-8530FPlus) with an accelerating voltage of 10 kV, a beam current of 40 nA, and a beam diameter of 0.5 µm. Data was acquired using analyzing crystals LDE1 for N-K_α and O-K_α, TAPL for Hf-M_α and Ta-M_α, and PETL for Mo-L_α, Nb-L_α, Ti-K_α, and Zr-L_α. Silicon nitride (Si_4N_3), hematite (α-Fe_2O_3), and pure metals of Hf, Mo, Nb, Ta, Ti, and Zr were used as standards for N, O, and the metals, respectively. Further analysis was performed using transmission electron microscope (TEM, Thermo Fisher TALOS FX200) operated at 200 kV. TEM lamellae were prepared using focused ion beam scanning electron microscopy (FIB-SEM, FEI Helios NanoLab G4 DualBeam).

Nanohardness and reduced modulus measurements were performed with a triboindenter (Bruker-Hysitron TI 980) equipped with a NanoDMA transducer and a diamond Berkovich probe. The tip area function of the indenter was calibrated utilizing a partial load-unload indent on a quartz calibration sample following the Oliver and Pharr method [57]. Indents were spaced 5 μm apart progressing radially from the nitrided surface inwards. For each sample, a total of 30 indents was performed, except for Ta samples, on which 60 indents were performed due to increased nitrogen diffusion length. Hardness and reduced modulus were measured as a function of indentation depth by NanoDMA with an oscillation frequency of 110 Hz. All indents followed a load-controlled strain-rate load function [58] , which incorporated a preload of 2 μN and maximum load of 12000 μN. The indentation strain rate used was 10^{-3} s^{-1}. An initial constant loading rate segment up to 1000 μN was used before the constant strain rate segment was initiated. Some edge rounding was observed at the interface between the samples and the mounting epoxy; thus, the hardness measurements of the points closest to the surface are less reliable than the points deeper into the metal.

3 RESULTS

3.1 Influence of time, temperature, and nitriding potential on mass gain

The square of the mass change per unit area of each set of samples is plotted as a function of time in **Figure 5**, and are fitted with a parabolic rate law:

$$\left(\frac{\Delta M}{A}\right)^2 = k_p \times t + C \tag{2}$$

where ΔM is the mass change, A is the sample surface area, k_p is the rate constant, t is time, and C is a constant to account for a change in mechanism at early stages of nitriding, or an incubation time. The fits shown in **Figure 5** have coefficients of determination (R^2 value) higher than 0.98, indicating that the mass changes conform to the parabolic law and suggesting diffusion control. Although only two experimental times were used to fit the 750 ºC data, the fact that the y-intercepts of those fits are close to zero (i.e. no mass gain at t = 0) supports the conclusion that the process also follows parabolic kinetics.

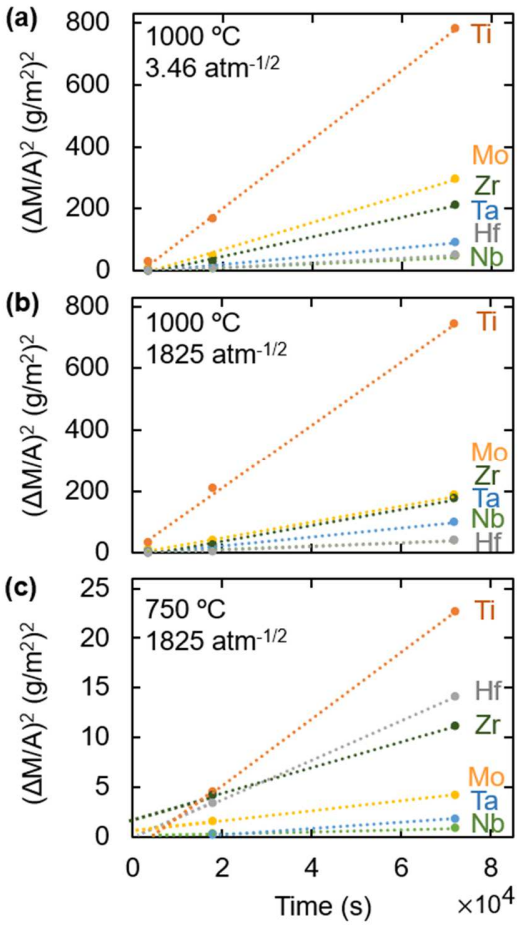

Figure 5. Mass gain for metals nitrided at (a) 1000 ºC, r_N = 3.46 $atm^{-1/2}$, (b) 1000 ºC, r_N = 1825 $atm^{-1/2}$, and (c) 750 ºC, r_N = 1825 $atm^{-1/2}$. The data are fitted with a parabolic rate law.

In **Figure 5** (a) and (b), the mass changes are similar for the two nitriding potentials, indicating that both r_N are sufficiently higher than the minimum r_N required to form nitrides (**Figure 4**) to minimize its influence on mass change. Conversely, temperature has a significant effect, with the mass change decreasing by an order of magnitude from 1000 ºC to 750 ºC (**Figure 5** (c)). Among the six elements, the mass change for Ti is much higher than the other elements especially at 1000 ºC. This could be related to the high solubility limit, high diffusion rate of nitrogen in Ti.

The parabolic rate constants (k_p) for mass gain are shown in **Figure 6** (a). At 1000 ºC, the rate constants are slightly smaller for the higher r_N. This could suggest that the increased surface nitrogen concentration at high r_N hastens formation of a nitride compound layer that acts as a diffusion barrier for nitrogen dissolution into the metal. The activation energies at r_N = 1825 $atm^{-1/2}$ were calculated using the rate constants for 750 ºC and 1000 ºC, assuming an Arrhenius rate

dependence for a single-step reaction and the same reaction mechanism at both temperatures. The activation energies (**Figure 6** (b)) fall in the range 140-180 kJ/mol, except for Hf, which is approximately a factor of four lower. This implies that temperature has a smaller influence on mass gain during nitriding for Hf. The comparable activation energies suggest a similar nitrogen diffusion mechanism except for Hf. As elaborated below, the difference for the latter is likely since it does not form an external nitride.

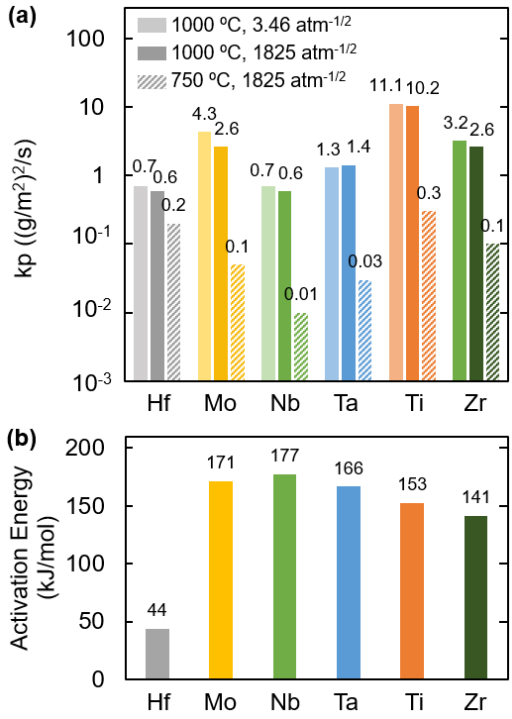

Figure 6. (a) Rate constants from the parabolic law at the three nitriding conditions and (b) activation energies calculated using the rate constants of the r_N = 1825 $atm^{-1/2}$ data.

3.2 Overview of Cross-Sectional Microstructure and Hardness Observations

This section provides an overview of the cross-sectional microstructure and hardness analysis. This initial discussion focuses on the 1000 ºC, 20 h samples, which showed the most pronounced reaction layers. The effects of time, temperature, and nitriding potential on the behavior of each metal are described in subsequent sections. **Figure 7** shows photographs, micrographs, and subsurface composition profiles measured by WDS for the samples nitrided at 1000 ºC and an r_N of 1825 $atm^{-1/2}$ for 20 hrs. The initial surface appearances were all metallic gray. After nitriding, the colors changes to blue, white, or yellow, and the samples became more dull. Moving from left to right, each BS-SEM image shows the epoxy (black), then the nitrides (darker gray), and

finally the diffusion zone and the pure metal substrate (brighter gray). In some cases, multiple nitride layers can be distinguished based on their relative grayscale values, e.g., the darker (higher-N) nitride and lighter (lower-N) nitrides formed on Nb.

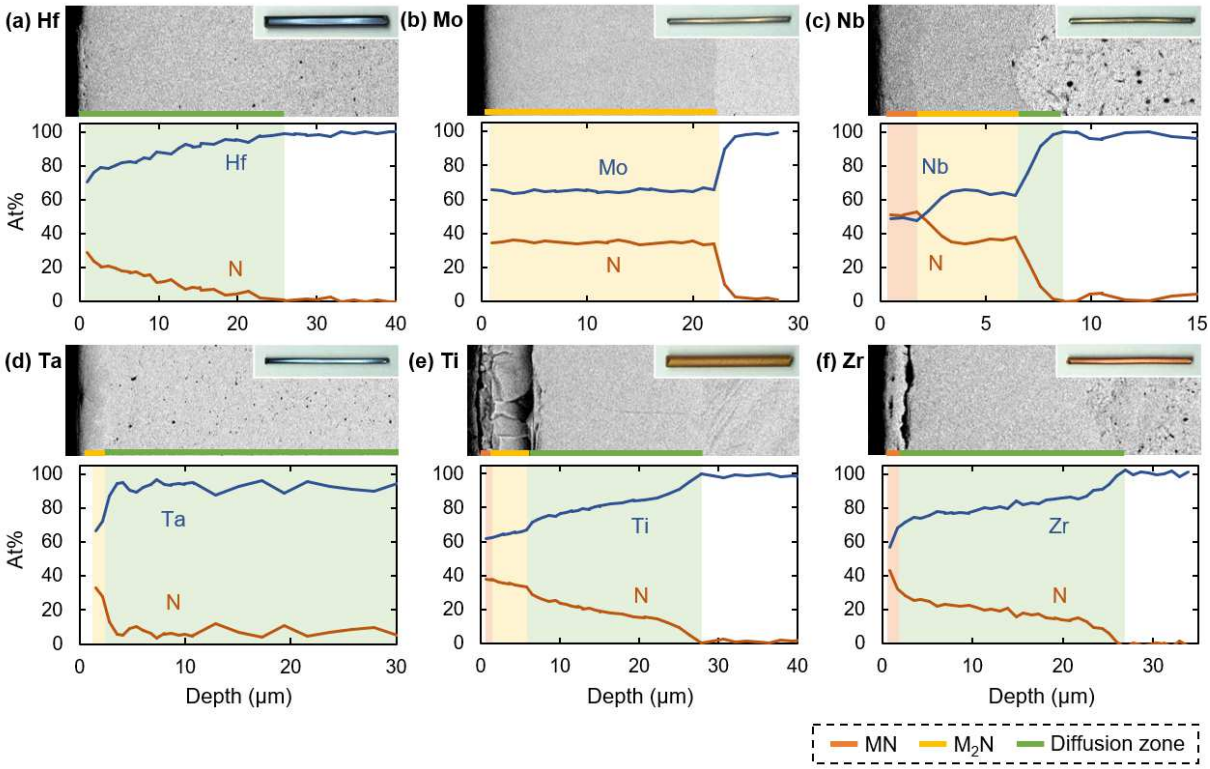

Figure 7. BS-SEM, WDS data, and surface appearance of (a) Hf, (b) Mo, (c) Nb, (d) Ta, (e) Ti, and (f) Zr nitrided at 1000 ºC, 20 h, r_N = 1825 $atm^{-1/2}$. The wires shown in the photographs are 20 mm long. The micrograph scale matches the composition depth axis. Each zone is colored based on the measured nitrogen content and the relative BSE contrast.

The BS-SEM images show that Mo, Nb, and Ta form dense and well-adhered nitride compound layers. No nitride layer is visible for Hf, and cracking and partial delamination of the surface layer occurred for Ti and Zr. The phases observed in BS-SEM were assigned according to WDS analyses and the phase diagrams in **Figure 3**. Mo and Ta formed M_2N-type (M: metal) nitrides and Zr formed an MN nitride. Nb and Ti formed outer MN-type and inner M_2N-type nitrides. No distinct nitride was formed on Hf; only a diffusion zone was observed. Hf, Ta, Ti, and Zr formed diffusion zones measuring several tens of μm thick. The diffusion zone for Nb was only a few μm thick, and no diffusion zone was discernable for Mo within the EPMA spatial resolution. The shape of the concentration profile for each material can be related to the corresponding phase equilibria. Hf, Ti, and Zr have nitrogen solubilities >20 at% at 1000 ºC, and the nitrogen

concentration decreases gradually from the nitride to pure metal. Conversely, the nitrogen concentration in Ta drops abruptly from the nitride to the metal solubility limit (5 at%), and remains ~5 at% for tens of µm implying full nitrogen saturation to a considerable depth. Finally, the limited diffusion zone in Mo and Nb is due to their near-zero solubility limits.

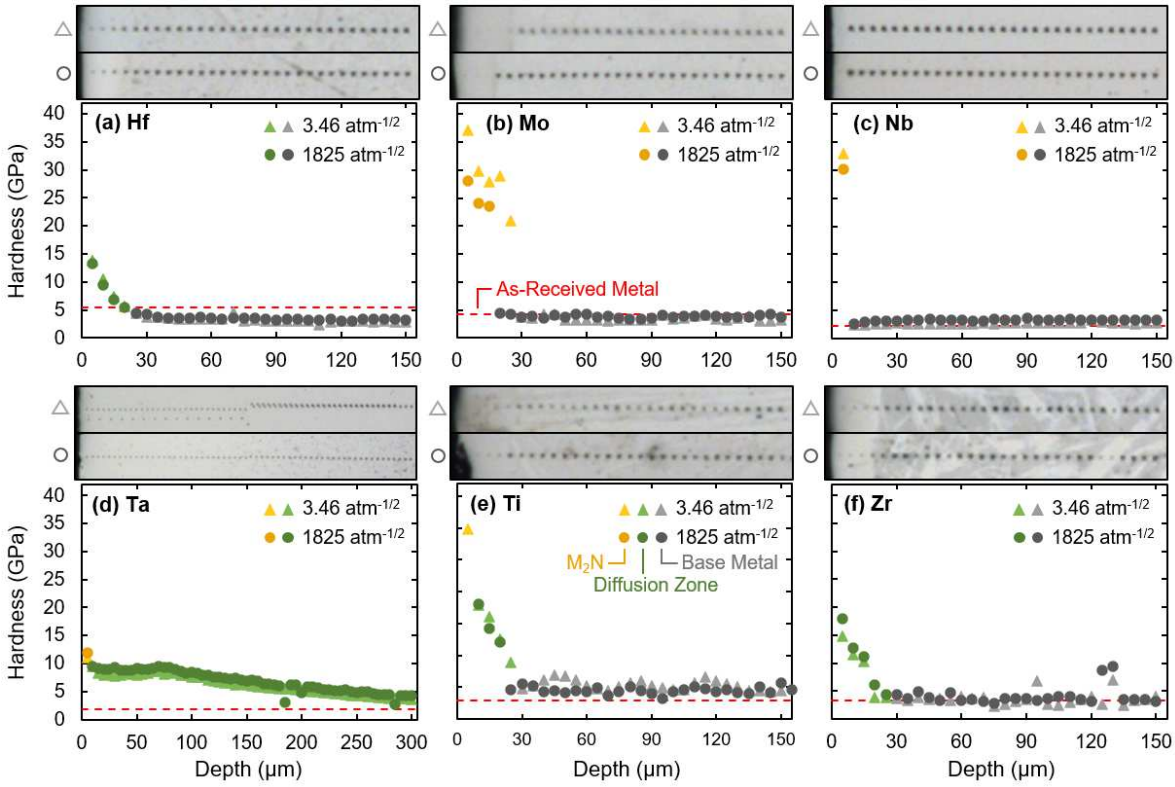

Figure 8. Hardness data of (a) Hf, (b) Mo, (c) Nb, (d) Ta, (e) Ti, and (f) Zr nitrided at 1000 ºC, 20 h, and r_N = 1825 $atm^{-1/2}$ or 3.46 $atm^{-1/2}$. The scale of the optical microscope images matches the depth axis. The symbol color corresponds to the zones identified based on the hardness values and comparison with the data in Figure 7.

Figure 8 shows the hardness data of the samples nitrided at 1000 ºC for 20 h. The results from the two nitriding potentials are similar, and the trends are consistent with the microstructure features shown in **Figure 7**. The nitride compound layers formed on Mo and Nb show high hardness (~25-35 GPa, with added uncertainty closest to the surface), followed by an abrupt drop in hardness to a level similar to the as-received metal. The nitride layers on Ta, Ti, and Zr were either too thin or cracked to measure the hardness conclusively. Along with Hf, these metals show increased hardness in the diffusion zone, with the highest hardness near the surface. The hardness decreases through the diffusion zone before reaching that of the as-received metal at the end of the diffusion layer. This behavior is consistent with the role of increased interstitial

nitrogen restricting the movement of dislocations, and leading to higher hardness. Fluctuations in the base-metal hardness for Zr (and, to a lesser extent, Ti) are attributed to the presence of two phases in the base metal, which were also observed in the optical microscope images. These likely formed by partial phase transformation when cooling from 1000 ºC. **Figure 9** shows the relationship between nitrogen concentration and the increase in hardness (relative to the hardness of the metal outside the diffusion zone) for Hf, Zr, and Ti, which formed N-rich diffusion zones. The results show a roughly linear relationship (R^2 > 0.97 in each case) and similar slopes, although the absolute magnitude of the hardness increase is not the same for each metal.

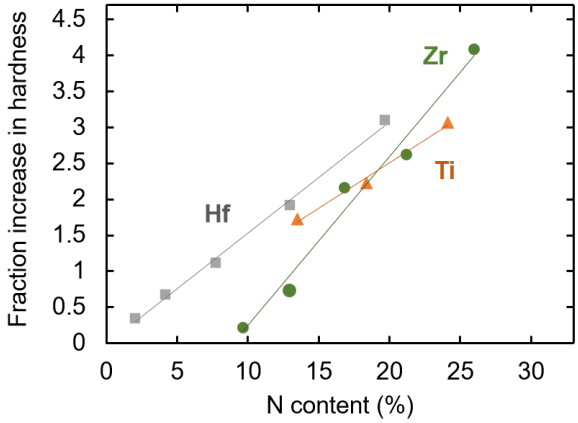

Figure 9. Effect of nitrogen content on increased hardness in the diffusion zone of the Hf, Zr, and Ti samples nitrided for 20 h at 1000 ºC and r_N = 1825 $atm^{-1/2}$. The y-intercepts of the fitting lines of Ti and Zr are not zero due to the fact that for Zr and Ti the nitrogen content drops quickly in the last few micrometers adjacent to the base metal.

3.3 Microstructural analysis of individual metals

The following sections the nitridation of each metal, including comparison with observations reported in the literature.

3.3.1 Nitridation of Hafnium

The Hf microstructures show no evidence of nitride phases, regardless of the nitriding time or temperature (**Figure 10** (a)). The corresponding WDS data (**Figure 10** (b)) shows the diffusion depths and the nitrogen contents at the surface increase with time. The surface concentration only approaches the solubility limit after 20 h at 1000 ºC. This implies that the rate of inward diffusion outpaces nitrogen dissolution at the surface. This prevents the nitrogen content from reaching the level to form a nitride compound. The 750 ºC, 20 h sample shows only a small

nitrogen content at the first measurable point, meaning that the nitrogen diffusion rate drops significantly with temperature.

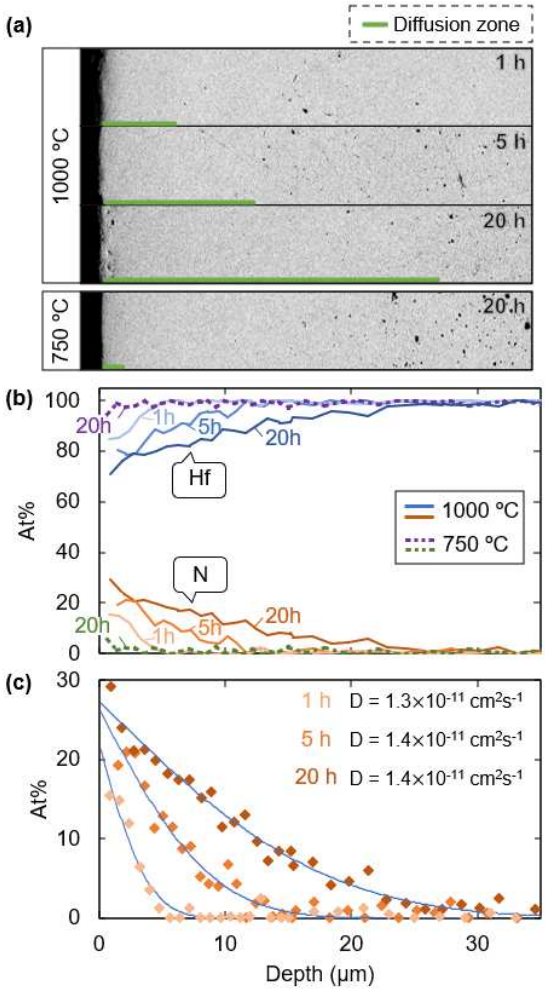

Figure 10. (a) BS-SEM, (b) WDS data showing the Hf and N concentration profiles, and (c) fits of the nitrogen concentration profiles for the 1000 ºC, r_N = 1825 $atm^{-1/2}$ data used to calculate the nitrogen diffusivity in Hf.

The nitrogen concentration profile data for the 1000 ºC samples was fit using a solution of Fick's second law:

$$\frac{dc_N(x,t)}{dt} = D\frac{d^2c_N(x,t)}{dx^2} \tag{3}$$

$$c_N = C_0 \times \mathrm{erfc}\left(\frac{x}{2\sqrt{D\times t}}\right) \tag{4}$$

where c_N is the nitrogen concentration in the matrix, t is the nitriding time, D is the diffusivity of atomic nitrogen in the metal, x is the depth from the surface, and C_0 is the nitrogen concentration at $x = 0$. **Figure 10** (c) shows that the data is well-fit ($R^2 > 0.95$) with D of 1.3×10^{-11}, 1.4×10^{-11} and 1.4×10^{-11} cm^2/s for 1, 5, and 20 h, respectively. The diffusivities obtained from the three cases are almost the same and similar to literature [60].

3.3.2 Nitridation of Molybdenum

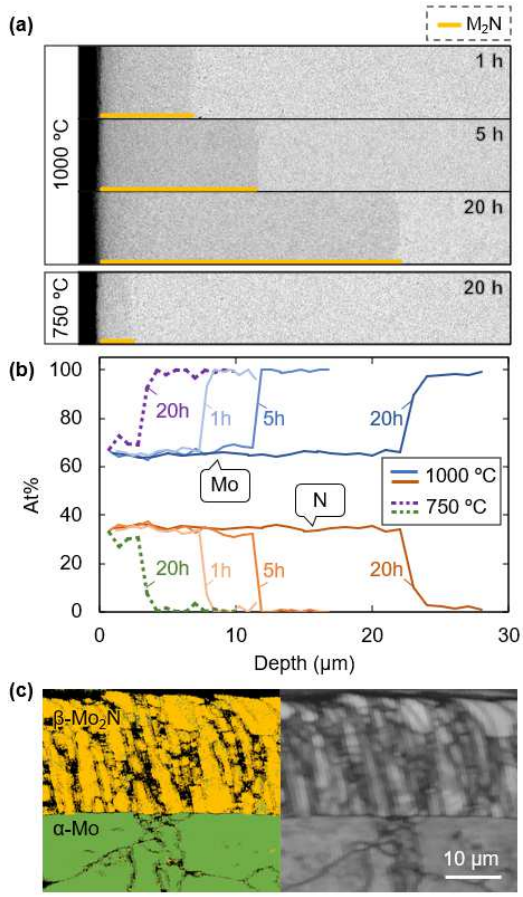

Figure 11. (a) BS-SEM and (b) WDS data of Mo nitrided at $r_N = 1825$ atm$^{-1/2}$ showing formation of Mo_2N nitride and abrupt change in nitrogen content between zones, and (c) EBSD phase ID and image quality maps of the same cross section location showing surface layer of Mo nitrided at 1000 ºC, 20 h, $r_N = 1825$ atm$^{-1/2}$.

Figure 11 (a,b) shows that the thickness of the single nitride formed on the Mo surface increases with time. This layer is dense with a smooth interface between the nitride and metal. The WDS data shows that this layer uniformly contains ~66% Mo and ~33%N, i.e. Mo_2N. The EBSD data from the 1000 ºC, 20 h sample shows that this is β-Mo_2N with small columnar grains compared to the grain size of the base metal. γ-Mo_2N was expected at 1000 ºC based on **Figure 3** and may

have transformed to β upon cooling. This result is also different from studies by Nagae et al. [49] and Martinz et al. [50], who observed either a composite of γ-Mo_2N and β-Mo_2N, or only γ-Mo_2N. A possible reason is that the slower cooling rate used in this work allowed time for the γ-to-β transformation. At 750 ºC, the N content is slightly lower, but still within the range of Mo_2N in the phase diagram. The WDS data shows that nitrogen content drops abruptly from ~33% to almost zero at the interface between the nitride and the base metal, consistent with the negligible nitrogen solubility in Mo.

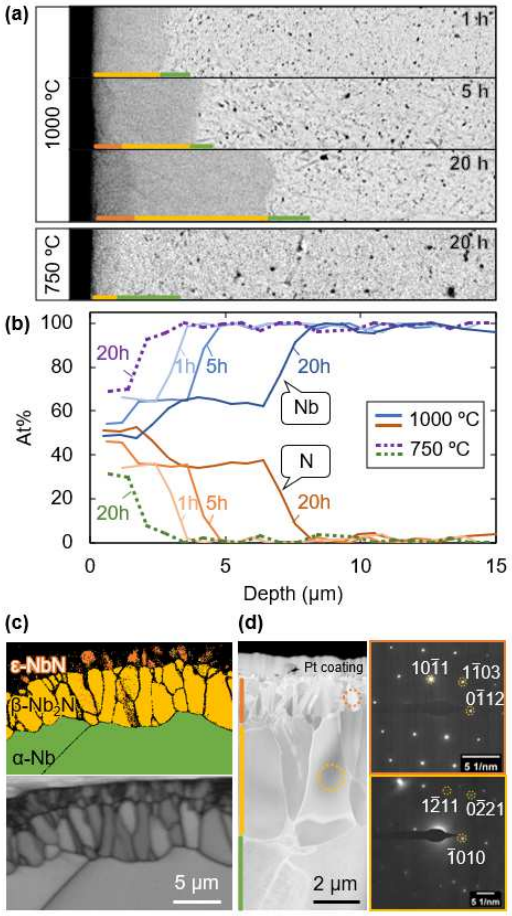

Figure 12. (a) BS-SEM and (b) WDS data of Nb nitrided at r_N = 1825 $atm^{-1/2}$ showing the formation of dense M_2N and MN nitrides at the higher temperature. (c) EBSD phase ID and image quality maps and (d) HAADF-STEM image and selected area diffraction pattern of Nb nitrided at 1000 ºC, 20 h, r_N = 1825 $atm^{-1/2}$. Lower EBSD pattern quality for the ε-NbN layer resulted in poor indexing for many ε-NbN grains. The depth of the measurable nitrogen diffusion in α-Nb is less than the grain size shown in (c).

3.3.3 Nitridation of Niobium

Figure 12 (a) shows the microstructure of the nitrided Nb samples. The compound layers are dense and adherent. Two layers are clearly evident for the 1000 ºC samples nitrided for 5 h and

20 h, and are likely also present after 1 h. The WDS data in **Figure 12** (b) shows that the outer nitride is NbN and the inner nitride is Nb_2N. The nitrogen content then drops rapidly to near zero. Although the nitrogen solubility limit (1 at %) is near the detection limit for EPMA, the fact that the hardness also drops to that of the as-received alloy at the point provides additional evidence that the diffusion zone depth is limited. At 750 ºC, only Nb_2N was observed in the compound layer based on the SEM and EPMA characterization.

The EBSD and TEM results (**Figure 12** (c,d)) show that the nitrides in the 1000 ºC, 20 h sample are β-Nb_2N and ε-NbN. The nitride grains are columnar, and the grain size decreases from the pure metal to the β-Nb_2N and finally to ε-NbN. The identity of the ε-NbN was further verified using TEM selected area diffraction patterns due to difficulties in obtaining damage-free surfaces suitable for EBSD. The γ-Nb_4N_3 phase was not detected in these samples. Although this phase is shown in one version of the Nb-N phase diagram [32,34], other studies did not find γ-Nb_4N_3 [29].

3.3.4 Nitridation of Tantalum

Figure 13 (a) shows the microstructures of the nitrided Ta. There is no detectable nitride at the surface of the 750 ºC sample. The nitride layers observed at the surface of each 1000 ºC sample thicken with time, but remain thinner than on the other metals. According to **Figure 3**(d), the nitrogen content of the Ta_2N phase ranges from 24 to 33% at both 750 and 1000 ºC, and the solubility limits in BCC Ta are 3 and 5%, respectively. The WDS data in **Figure 13**(b) shows that the nitrogen content at the surface of the 1000 ºC, 20 h samples is consistent with the N-rich limit for Ta_2N. For the 1000 ºC, 5 h and 20 h samples, the highest nitrogen contents at the surface are both lower than the N-lean limit for Ta_2N, but higher than the solubility limit. It is speculated that there is a Ta_2N layer at the surface of both samples, but it is too thin to measure via WDS. The diffusion zone for Ta extended much further into the metal than the diffusion zones in the high solubility Hf, Ti, and Zr. At 750 ºC, the diffusion zone is about 25 µm thick, compared to only a few µm for the other metals. For the 1000 ºC samples, the WDS data shows a uniform nitrogen content near the 5 at% solubility limit to a depth greater than 30 µm. The hardness profile in **Figure 8** is constant for the first 70 µm and then drops slowly to the baseline at a depth of 220 µm. This implies that the metal is saturated with nitrogen to a depth of 70 µm and the diffusion zone is over 200 µm thick (compared to a few tens of µm for the other metals).

These observations imply that nitrogen diffusion is fast in Ta, making it difficult to maintain a high surface nitrogen content to form nitrides before nitrogen diffuses into the metal interior.

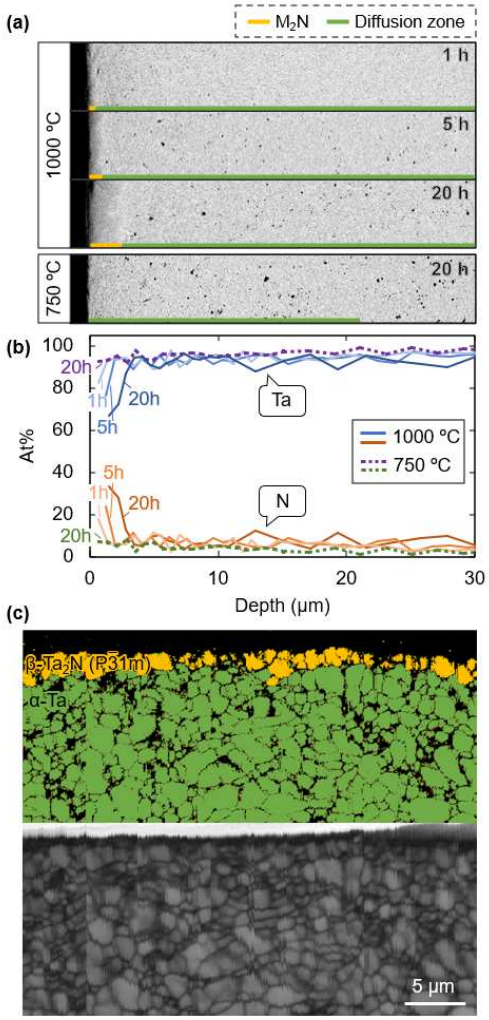

Figure 13. (a) BS-SEM and (b) WDS data of Ta nitrided at r_N = 1825 $atm^{-1/2}$ confirming the existence of a Ta_2N phase and a large area with small but non-zero nitrogen content beneath the nitride phase, and (c) EBSD phase ID and image quality maps of Ta nitrided at 1000 ºC, 20 h, r_N = 1825 $atm^{-1/2}$.

The EBSD analysis showed that the Ta_2N layer is either P$\bar{3}$m1 or P$\bar{3}$1m. The two are not readily distinguished by diffraction, so P$\bar{3}$1m was assigned in **Figure 13** (c) based on reports noting that it is more stable than P$\bar{3}$m1 [61]. This result is inconsistent with the phase diagram, which shows that the only Ta_2N phase is γ-Ta_2N ($P6_3/mmc$). In fact, both space groups appeared in different literature [61–64] to describe the structure of γ-Ta_2N. P$\bar{3}$m1 phase is similar to $P6_3/mmc$ by alternating filled and empty prisms in neighboring layers in $P6_3/mmc$, while P$\bar{3}$1m, is a superlattice structure with a different arrangement of the nitrogen atoms.

3.3.5 Nitridation of Titanium

After gas nitriding, all Ti samples appeared golden, consistent with TiN [65]. The morphology of the cracked regions suggests that two distinct compound layers formed at 1000 ºC. The WDS data in **Figure 14** (b) shows that the outermost layer of the 20 h sample contains ~37% N, which is the N-lean limit of TiN at 1000 ºC. The layer underneath it has a nitrogen content of around 34%, i.e. Ti_2N. Although the combination of reduced thickness and cracking reduces the reliability of the WDS measurements for the two samples nitrided at 1000 ºC for a shorter time, they are consistent with the interpretation that the outer layer is TiN, and the inner layer is Ti_2N. The existence of a thin layer of TiN in all 1000 ºC is consistent with the large formation enthalpy of TiN [66,67]. As the TiN layer grows, it acts as a barrier to nitrogen dissolution [68]. A thin layer of TiN is present on the surface of the 750 ºC sample, with limited formation of Ti_2N. It is possible that the TiN layer in the 750 ºC sample is still not thick enough to make the nitrogen dissolution rate be slower than the diffusion rate nitrogen in the metal. The nitrogen content in the TiN layer (~41%) is also higher than that of the 1000 ºC samples (~37%), in agreement with the N-lean limit line in the phase diagram.

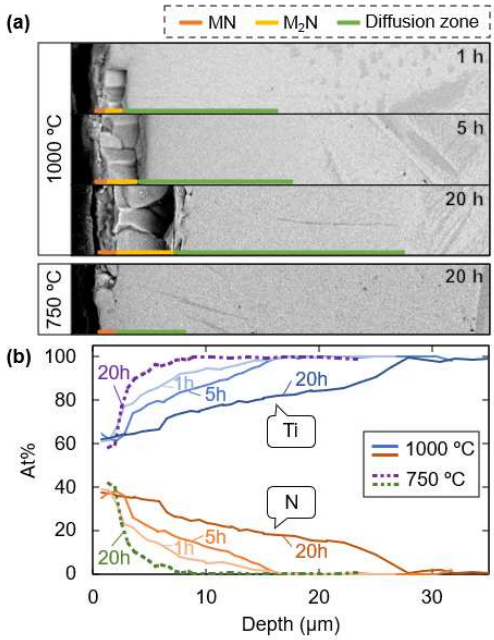

Figure 14. (a) BS-SEM and (b) WDS data of Ti nitrided at r_N = 1825 $atm^{-1/2}$ showing cracking, pullout, and partial delamination of the surface layers, the growth of the compound layers and diffusion zones, and the existence of a two-phase area in the core.

Figure 14 (a) shows that all titanium nitride layers are cracked and partially delaminated, although this is more severe in the 1000 ºC samples. The VERs of Ti_2N and TiN calculated based on α-Ti are 1.08 (in Table 1), and those based on β-Ti (density from [40]) are 1.05, suggesting limited growth stress. The linear CTEs of α-Ti [69], β-Ti [70], and TiN [71] are 10.5×10^{-6}, 13.8×10^{-6}, and 9.8×10^{-6} K^{-1}, respectively. One explanation of the more severe cracking and delamination at 1000 ºC samples is the CTE mismatch with the high-temperature β-Ti phase or a transformation strain during cooling. Another possible explanation could be CTE mismatch with the Ti_2N, for which CTE data is not readily available.

A thick diffusion zone developed under the compound layer for all of the Ti samples. The shape of the nitrogen profile in the diffusion zone is not consistent with the typical error function solution to Fick's Laws. Accumulation of higher nitrogen concentration adjacent to the base metal, which is especially obvious in the 1000 ºC 20 h sample, is likely due to the influence of nitrogen on the α-β phase transformation. Underneath the diffusion zone, a region with two different phases is observed in the BSE images, and the fluctuating hardness in this region in **Figure 8** (e) is also evidence. In this work, EBSD shows that the lamellae are α-Ti, so they are probably α-Ti with a small amount of dissolved nitrogen, giving rise to a higher hardness. This is consistent with previous observations [54] that showed a two-phase core structure of Ti nitrided with ammonia, thought to arise due to the interaction of hydrogen with the α-β phase transformation upon heating and cooling.

3.3.6 Nitridation of Zirconium

The surface nitride layer on the 1000 ºC Zr samples also spalled (**Figure 15**(a)), although the layer exhibited less cracking than the Ti samples. The WDS data (**Figure 15**(b)) suggests that the composition of the compound layer is ZrN. No spalling and no compound layer is observed in the 750 ºC sample. The cracking is attributed to a combination of the stress caused by the volumetric strain upon the formation of nitrides, and the thermal strain generated from the CTE mismatch during cooling. In this case, there is significant CTE mismatch with the linear CTE of Zr [72] and ZrN [73] being 5.84×10^{-6} and 8.39×10^{-6} K^{-1}, respectively.

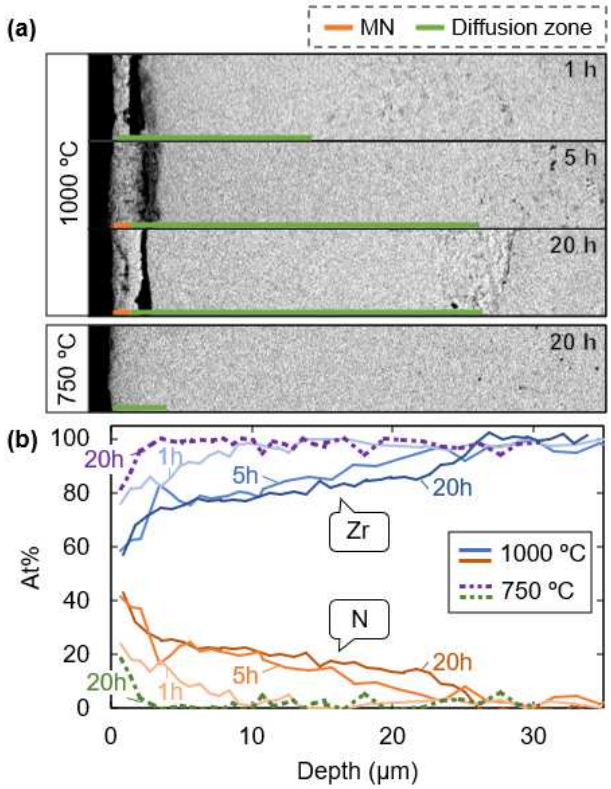

Figure 15. (a) BS-SEM and (b) WDS data of Zr nitrided at r_N = 1825 $atm^{-1/2}$ showing severe delamination of the surface layers at 1000 ºC, and the formation of large diffusion zones.

The nitrogen content in the 1000 ºC samples drops gradually from the solubility limit (~23%) to zero. The diffusion zone extends approximately 10 µm below the surface after 1 h, and from 20 to 30 µm after the longer times. The 750 ºC sample didn't reach the solubility limit (~22%) at its surface. The thickness of the diffusion zone is shallower at 750 ºC, implying a drop in the dissociation rate at a lower temperature. Accumulation of nitrogen at the interface of the diffusion zone and the substrate was observed in the 1000 ºC 20 h sample as in the Ti sample obtained with the same condition, perhaps due to the α-β phase transition.

4 DISCUSSION

The results provide insights to inform the design and processing of refractory-based MPEAs to facilitate nitridation to enhance the surface characteristics. For instance, an MPEA containing elements that can form a dense compound layer and elements that can form a deep diffusion zone would enable simultaneous tuning of the surface properties and the sub-surface hardness gradient.

The first consideration is the ability to form a dense, adherent, and crack-free nitride compound layer. At 1000 ºC, Mo, Nb, and Ta did this effectively, while Hf did not readily form a compound layer. The layers on Ti and Zr cracked or and delaminated. Nb and Ta were found to have similar M_2N in the compound layer, but very different diffusion zone depths. An alloy combining these could form $(Nb_xTa_{1-x})_2N$ with varying diffusion zone depths. Finally, in addition to Ti and Zr, the phase diagrams suggest that Hf, Nb, and Ta are all expected to be at least moderately stable in a rock-salt MN, providing opportunities to form a rock-salt structured solid solution nitride.

The second consideration is the development of the diffusion zone with sufficient thickness and near-surface hardness to support the surface compound layer and avoid premature spallation. In this respect, the alloys can be grouped into three categories. Hf, Ti, and Zr formed relatively shallow (10s of μm) but N-rich diffusion zones with peak hardness reaching 10 to 15 GPa. This is roughly half that of typical nitride compounds, and therefore would enable a gradual change in hardness across the interface and into the base alloy. Ta formed a deep (100s of μm), but low-N compound layer that would enable more gradual sub-surface hardness gradient but with lower peak hardness. Mo and Nb don't form a diffusion zone due to their low nitrogen solubility. Based on these results, one could design alloys employing Nb and Ta to form an adherent $(Nb_xTa_{1-x})_2N$ layer with a combination of higher-solubility elements to produce a near-surface hardness.

The final consideration is the selection of processing conditions. The results showed that the material response was relatively independent of r_N over a range relevant to efficient processing. The implication is that the nitrogen affinity of these metals is sufficiently high that the supply of nitrogen (as NH_3) in the gas phase is not a limiting factor. It is also found that the nitriding reaction rate is faster at 1000 ºC compared to 750 ºC. This means that higher temperatures (e.g.,1000 ºC) would be more suitable for nitriding MPEAs in cases where a thick compound layer is desired, while lower temperatures could provide benefits if it is desired to limit nitride formation and instead surface harden primarily via interstitial nitrogen in the diffusion zone. A lower temperature with a subsequent higher temperature can also be considered for MPEAs that form nitrides faster than the development of a diffusion zone. This may provide enough time for nitrogen diffusion before the formation of thick nitride layers that hinder nitrogen penetration.

The activity of each element in an MPEA will vary with its concentration and the overall alloy constitution. The activity changes the tendency of nitride formation of each alloying element under a given set of processing conditions. By mixing elements having nitrides with similar structures and tuning their concentrations to make the Gibb's free energies of nitride formation comparable, it would be possible to form solid solution nitrides. Thus, the results from this work can be readily integrated with computational thermodynamics models of alloy reactivity to guide the selection of elements in future MPEA design.

5 CONCLUSIONS

The nitriding behavior of six refractory metals (Hf, Mo, Nb, Ta, Ti, and Zr) was studied to provide complimentary structural-property information for MPEA design. The conclusions are:

1. The nitriding mass gain for all six elements follows parabolic kinetics. Both nitriding potentials studied at 1000 ºC produce similar results, but the mass gain and the thickness of the nitrided zone are greater at 1000 ºC than 750 ºC.
2. The nitride layers formed on Mo, Nb, and Ta are dense and adhered, while delamination occurs for Ti and Zr. Hf did not form an outer nitride compound layer.
3. Hf, Ti, and Zr, which have relatively high nitrogen solubilities (23 to 28 at%), each form ~25 μm thick diffusion zones after nitriding for 20 h at 1000 ºC. Ta, which has a lower solubility limit (5 at%), formed a thicker diffusion zone up to 220 μm thick. The implication is that nitrogen diffusion in Ta is comparatively fast.
4. The shape of the hardness profiles is similar to the nitrogen content profile, and the thickness of the nitrided zones obtained from both sets of data are consistent. The nitrides can have hardness values up to 30 GPa. The hardness within the diffusion zone can increase by up to 5 times relative to the pure metals.

6 ACKNOWLEDGEMENTS

This research was supported by the Office of Naval Research (ONR) award N00014-20-1-2732, monitored by Dr. David Shifler. J.Y. Cheng is supported in part by DOE NNSA under cooperative agreement number DE-NA0003960. The shared equipment used in this work is supported by NSF MRI DMR-1229263 (Hitachi SU8230), NSF EAR-1625422 (EPMA). SEM-EBSD, TEM characterization, and hardness measurements were carried out in the

Characterization Facility, University of Minnesota, a member of the Materials Research Facilities Network (www.mrfn.org), which is partially supported by the NSF through the MRSEC (Award Number DMR-2011401) and the NNCI (Award Number ECCS-2025124) programs. The authors are grateful to Dr. Nicholas Seaton for EBSD assistance.

REFERENCES

[1] O.N.Senkov, G.B.Wilks, D.B.Miracle, C.P.Chuang, P.K.Liaw, Refractory high-entropy alloys, Intermetallics. 18 (2010) 1758–1765. https://doi.org/https://doi.org/10.1016/j.intermet.2010.05.014.

[2] O.N.Senkov, C.F.Woodward, Microstructure and properties of a refractory $NbCrMo_{0.5}Ta_{0.5}TiZr$ alloy, Mater. Sci. Eng. A. 529 (2011) 311–320. https://doi.org/10.1016/J.MSEA.2011.09.033.

[3] V.Kumar, A.Gupta, D.Lahiri, K.Balani, Serrated yielding during nanoindentation of thermomechanically processed novel Mg–9Li–7Al–1Sn and Mg–9Li–5Al–3Sn–1Zn alloys, J. Phys. D. Appl. Phys. 46 (2013) 145304. https://doi.org/10.1088/0022-3727/46/14/145304.

[4] D.B.Miracle, J.D.Miller, O.N.Senkov, C.Woodward, M.D.Uchic, J.Tiley, Exploration and development of high entropy alloys for structural applications, Entropy. 16 (2014). https://doi.org/10.3390/e16010494.

[5] X.Yang, S.Y.Chen, J.D.Cotton, Y.Zhang, Phase stability of low-density, multiprincipal component alloys containing aluminum, magnesium, and lithium, JOM. 66 (2014) 2009–2020. https://doi.org/10.1007/s11837-014-1059-z.

[6] M.Z.Ghomsheh, G.Khatibi, B.Weiss, M.Lederer, S.Schwarz, A.Steiger-Thirsfeld, M.A.Tikhonovsky, E.D.Tabachnikova, E.Schafler, High cycle fatigue deformation mechanisms of a single phase CrMnFeCoNi high entropy alloy, Mater. Sci. Eng. A. 777 (2020) 139034. https://doi.org/10.1016/J.MSEA.2020.139034.

[7] D.B.Miracle, O.N.Senkov, A critical review of high entropy alloys and related concepts, Acta Mater. 122 (2017) 448–511. https://doi.org/10.1016/j.actamat.2016.08.081.

[8] H.Y.Diao, R.Feng, K.A.Dahmen, P.K.Liaw, Fundamental deformation behavior in high-entropy alloys: An overview, Curr. Opin. Solid State Mater. Sci. 21 (2017) 252–266. https://doi.org/10.1016/j.cossms.2017.08.003.

[9] E.H.Sirvio, M.Sulonen, H.Sundquist, Abrasive wear of ion-plated titanium nitride coatings on plasma-nitrided steel surfaces, Thin Solid Films. 96 (1982) 93–101. https://doi.org/10.1016/0040-6090(82)90217-6.

[10] V.Braic, A.Vladescu, M.Balaceanu, C.R.Luculescu, M.Braic, Nanostructured multi-element (TiZrNbHfTa)N and (TiZrNbHfTa)C hard coatings, Surf. Coatings Technol. 211 (2012) 117–121. https://doi.org/10.1016/J.SURFCOAT.2011.09.033.

[11] Q.Yang, L.R.Zhao, P.C.Patnaik, X.T.Zeng, Wear resistant TiMoN coatings deposited by magnetron sputtering, Wear. 261 (2006) 119–125. https://doi.org/10.1016/J.WEAR.2005.07.008.

[12] V.V.Uglov, V.M.Anishchik, S.V.Zlotski, G.Abadias, S.N.Dub, Structural and mechanical stability upon annealing of arc-deposited Ti–Zr–N coatings, Surf. Coatings Technol. 202 (2008) 2394–2398. https://doi.org/10.1016/J.SURFCOAT.2007.09.035.

[13] A.Nishimoto, T.Fukube, T.Maruyama, Microstructural, mechanical, and corrosion properties of plasma-nitrided CoCrFeMnNi high-entropy alloys, Surf. Coatings Technol. 376 (2019) 52–58. https://doi.org/10.1016/j.surfcoat.2018.06.088.

[14] T.Karimoto, A.Nishimoto, Plasma-nitriding properties of CoCrFeMnNi high-entropy alloys produced by spark plasma sintering, Metals (Basel). 10 (2020) 761–772. https://doi.org/10.3390/met10060761.

[15] Y.Wang, Y.Yang, H.Yang, M.Zhang, S.Ma, J.Qiao, Microstructure and wear properties of nitrided AlCoCrFeNi high-entropy alloy, Mater. Chem. Phys. 210 (2018) 233–239. https://doi.org/10.1016/j.matchemphys.2017.05.029.

[16] J.Hou, W.Song, L.Lan, J.Qiao, Surface modification of plasma nitriding on $Al_xCoCrFeNi$ high-entropy alloys, J. Mater. Sci. Technol. 48 (2020) 140–145. https://doi.org/10.1016/j.jmst.2020.01.057.

[17] Y.Wang, Y.Yang, H.Yang, M.Zhang, J.Qiao, Effect of nitriding on the tribological properties of $Al_{1.3}CoCuFeNi_2$ high-entropy alloy, J. Alloys Compd. 725 (2017) 365–372. https://doi.org/10.1016/j.jallcom.2017.07.132.

[18] W.Y.Tang, J.W.Yeh, Effect of aluminum content on plasma-nitrided $Al_xCoCrCuFeNi$ high-entropy alloys, Metall. Mater. Trans. A Phys. Metall. Mater. Sci. 40 (2009) 1479–1486. https://doi.org/10.1007/s11661-009-9821-5.

[19] W.-Y.Tang, M.-H.Chuang, S.-J.Lin, J.-W.Yeh, Microstructures and mechanical performance of plasma-nitrided $Al_{0.3}CrFe_{1.5}MnNi_{0.5}$ high-entropy alloys, Metall. Mater. Trans. A. 43 (2012) 2390–2400. https://doi.org/10.1007/s11661-012-1108-6.

[20] W.Y.Tang, M.H.Chuang, H.Y.Chen, J.W.Yeh, Microstructure and mechanical performance of new $Al_{0.5}CrFe_{1.5}MnNi_{0.5}$ high-entropy alloys improved by plasma nitriding, Surf. Coatings Technol. 204 (2010) 3118–3124. https://doi.org/10.1016/j.surfcoat.2010.02.045.

[21] W.Wang, S.Song, K.M.Reddy, W.Li, P.Liu, X.Wang, Deformation behavior of ultrahard $Al_{0.3}CoCrFeNi$ high-entropy alloy treated by plasma nitriding, Mater. Lett. 255 (2019) 126566. https://doi.org/10.1016/j.matlet.2019.126566.

[22] L.W.Lan, X.J.Wang, R.P.Guo, H.J.Yang, J.W.Qiao, Effect of environments and normal loads on tribological properties of nitrided $Ni_{45}(FeCoCr)_{40}(AlTi)_{15}$ high-entropy alloys, J. Mater. Sci. Technol. 42 (2020) 85–96. https://doi.org/10.1016/j.jmst.2019.08.051.

[23] A.D.Pogrebnjak, I.VYakushchenko, G.Abadias, P.Chartier, O.VBondar, V.M.Beresnev, Y.Takeda, O.VSobol', K.Oyoshi, A.A.Andreyev, B.A.Mukushev, The effect of the deposition parameters of nitrides of high-entropy alloys (TiZrHfVNb)N on their structure, composition, mechanical and tribological properties, J. Superhard Mater. 35 (2013) 356–368. https://doi.org/10.3103/S106345761306004X.

[24] S.A.Firstov, V.F.Gorban', N.I.Danilenko, M.VKarpets, A.A.Andreev, E.S.Makarenko, Thermal stability of superhard nitride coatings from high-entropy multicomponent Ti–V–Zr–Nb–Hf alloy, Powder Metall. Met. Ceram. 52 (2014) 560–566. https://doi.org/10.1007/s11106-014-9560-z.

[25] V.Gorban', I.Zakiev, G.Sarzhan, Comparative friction characteristics of high-entropy mononitride coatings, J. Frict. Wear. 37 (2016) 263–267. https://doi.org/10.3103/S1068366616030077.

[26] T.Makishi, K.Nakata, Surface hardening of nickel alloys by means of plasma nitriding, Metall. Mater. Trans. A. 35 (2004) 227–238. https://doi.org/10.1007/s11661-004-0123-7.

[27] Y.Chen, T.Laha, K.Balani, A.Agarwal, Nanomechanical properties of hafnium nitride coating, Scr. Mater. 58 (2008) 1121–1124. https://doi.org/10.1016/J.SCRIPTAMAT.2008.02.012.

[28] K.Khojier, M.R.K.Mehr, H.Savaloni, Annealing temperature effect on the mechanical and tribological properties of molybdenum nitride thin films, J. Nanostructure Chem. 3 (2013) 5. https://doi.org/10.1186/2193-8865-3-5.

[29] C.Borcz, C.M.Lepienski, S.F.Brunatto, Surface modification of pure niobium by plasma nitriding, Surf. Coatings Technol. 224 (2013) 114–119. https://doi.org/10.1016/J.SURFCOAT.2013.03.008.

[30] Z.Kolozsváry, Nitriding structure and properties of nitrided layers, in: J.L.Dossett, G.E.Totten (Eds.), Heat Treat. Irons Steels, ASM International, 2014: pp. 88–96. https://doi.org/10.31399/asm.hb.v04d.a0005986.

[31] H.Okamoto, The Hf-N (Hafnium-Nitrogen) system, Bull. Alloy Phase Diagrams. 11 (1990) 146–149. https://doi.org/10.1007/BF02841699.

[32] H.Okamoto, M.E.Schlesinger, E.M.Mueller, eds., ASM Handbook, Volume 3: Alloy Phase Diagrams, ASM International, Materials Park, OH, 1992.

[33] H.Jehn, P.Ettmayer, The molybdenum-nitrogen phase diagram, J. Less Common Met. 58 (1978) 85–98. https://doi.org/10.1016/0022-5088(78)90073-5.

[34] V.N.Zhitomirsky, I.Grimberg, L.Rapoport, N.A.Travitzky, R.L.Boxman, S.Goldsmith, A.Raihel, I.Lapsker, B.Z.Weiss, Structure and mechanical properties of vacuum arc-deposited NbN coatings, Thin Solid Films. 326 (1998) 134–142. https://doi.org/10.1016/S0040-6090(98)00544-6.

[35] K.Frisk, Analysis of the phase diagram and thermochemistry in the Ta–N and the Ta–C–N systems, J. Alloys Compd. 278 (1998) 216–226. https://doi.org/10.1016/S0925-8388(98)00582-9.

[36] H.Okamoto, N-Ta (Nitrogen-Tantalum), J. Phase Equilibria Diffus. 29 (2008) 291. https://doi.org/10.1007/s11669-008-9316-x.

[37] P.Franke, D.Neuschütz, N-Ti, in: P.Franke, D.Neuschütz (Eds.), Binary Systems. Part 4: Binary Systems from Mn-Mo to Y-Zr. Part of Landolt-Börnstein - Group IV Physical Chemistry, Springer-Verlag, Berlin, Heidelberg, 2006: pp. 1–2. https://doi.org/10.1007/10757285_21.

[38] T.B.Massalski, H.Okamoto, Pr.Subramanian, L.Kacprzak, W.W.Scott, Binary alloy phase diagrams, ASM International, Metals Park, OH, 1986.

[39] K.Anderson, J.Weritz, J.G.Kaufman, eds., ASM Handbook, Volume 2A: Aluminum Science and Technology, ASM International, Materials Park, OH, 2018.

[40] P.Villars, K.Cenzual, R.Gladyshevskii, eds., Handbook of Inorganic Substances 2016, De Gruyter, Berlin, 2016.

[41] C.L.Yaws, ed., Yaws' Critical Property Data for Chemical Engineers and Chemists, Knovel, Norwich, NY, 2012.

[42] S.Adachi, ed., The Handbook on Optical Constants of Metals: In Tables and Figures, World Scientific, Singapore, 2012.

[43] P.Kochmański, J.Nowacki, Activated gas nitriding of 17-4 PH stainless steel, Surf. Coatings Technol. 200 (2006) 6558–6562. https://doi.org/10.1016/J.SURFCOAT.2005.11.034.

[44] M.Hernandez, M.H.Staia, E.S.Puchi-Cabrera, Evaluation of microstructure and mechanical properties of nitrided steels, Surf. Coatings Technol. 202 (2008) 1935–1943. https://doi.org/10.1016/J.SURFCOAT.2007.08.018.

[45] J.R.Davis, Surface Hardening of Steels, first ed., ASM International, Ohio, 2002. https://doi.org/10.1361/shos2002p001.

[46] E.J.Mittemeijer, J.T.Slycke, Chemical potentials and activities of nitrogen and carbon imposed by gaseous nitriding and carburising atmospheres, Surf. Eng. 12 (1996) 152–162. https://doi.org/10.1179/sur.1996.12.2.152.

[47] R.K.Edwards, G.T.Malloy, The rate of reaction of nitrogen with hafnium metal, J. Phys. Chem. 62 (1958) 45–47. https://doi.org/10.1021/j150559a012.

[48] W.Lengauer, D.Rafaja, R.Täubler, C.Kral, P.Ettmayer, Preparation of binary single-phase line compounds via diffusion couples: The subnitride phases η-Hf_3N_{2-x} and ζ-Hf_4N_{3-x}, Acta Metall. Mater. 41 (1993) 3505–3514. https://doi.org/10.1016/0956-7151(93)90230-P.

[49] M.Nagae, S.Okada, M.Nakanishi, J.Takada, Y.Hiraoka, Y.Takemoto, M.Hida, H.Kuwahara, M.K.Yoo, Nitriding of dilute Mo-Ti alloys at a low temperature of 1373 K, Int. J. Refract. Met. Hard Mater. 16 (1998) 127–132. https://doi.org/10.1016/S0263-4368(98)00005-5.

[50] H.P.Martinz, K.Prandini, The carburization and nitriding of molybdenum and TZM, Int. J. Refract. Met. Hard Mater. 12 (1993) 179–186. https://doi.org/10.1016/0263-4368(93)90046-I.

[51] Y.Ufuktepe, A.H.Farha, S.I.Kimura, T.Hajiri, F.Karadağ, M.A.AlMamun, A.A.Elmustafa, G.Myneni, H.E.Elsayed-Ali, Structural, electronic, and mechanical properties of niobium nitride prepared by thermal diffusion in nitrogen, Mater. Chem. Phys. 141 (2013) 393–400. https://doi.org/10.1016/J.MATCHEMPHYS.2013.05.029.

[52] W.Lengauer, M.Bohn, B.Wollein, K.Lisak, Phase reactions in the Nb–N system below 1400°C, Acta Mater. 48 (2000) 2633–2638. https://doi.org/10.1016/S1359-6454(00)00056-2.

[53] D.A.Prokoshkin, T.A.Voronova, A.S.Gorbova, V.N.Kashirtsev, Nitriding of tantalum, Met. Sci. Heat Treat. 26 (1984) 357–360. https://doi.org/10.1007/BF00707409.

[54] P.K.Ajikumar, M.Kamruddin, R.Nithya, P.Shankar, S.Dash, A.K.Tyagi, B.Raj, Surface nitridation of Ti and Cr in ammonia atmosphere, Scr. Mater. 51 (2004) 361–366. https://doi.org/10.1016/J.SCRIPTAMAT.2004.05.024.

[55] M.Yoshida, R.Ichiki, N.Utsumi, Surface hardening of titanium using gas nitriding, Int. J. Precis. Eng. Manuf. 14 (2013) 971–976. https://doi.org/10.1007/s12541-013-0128-5.

[56] N.C.Reger, V.K.Balla, M.Das, A.K.Bhargava, Wear and corrosion properties of in-situ grown zirconium nitride layers for implant applications, Surf. Coatings Technol. 334 (2018) 357–364. https://doi.org/10.1016/J.SURFCOAT.2017.11.064.

[57] W.C.Oliver, G.M.Pharr, An improved technique for determining hardness and elastic modulus using load and displacement sensing indentation experiments, J. Mater. Res. 7 (1992) 1564–1583. https://doi.org/10.1557/JMR.1992.1564.

[58] K.M.Schmalbach, N.A.Mara, Algorithms for nanoindentation strain rate jump testing and analysis, Exp. Mech. 62 (2022) 885–888. https://doi.org/10.1007/s11340-022-00833-x.

[59] C.W.Bale, E.Bélisle, P.Chartrand, S.A.Decterov, G.Eriksson, A.E.Gheribi, K.Hack, I.H.Jung, Y.B.Kang, J.Melançon, A.D.Pelton, S.Petersen, C.Robelin, J.Sangster, P.Spencer, M.A.VanEnde, FactSage thermochemical software and databases - 2010 - 2016, Calphad. 54 (2016) 35–53.

[60] A.O'Hara, A.A.Demkov, Oxygen and nitrogen diffusion in α-hafnium from first principles, Appl. Phys. Lett. 104 (2014) 211909. https://doi.org/10.1063/1.4880657.

[61] L.Zhu, J.Wang, C.Dong, Y.Du, S.-L.Shang, Z.-K.Liu, Stability, elastic and electronic properties of Ta_2N by first-principles calculations, Crystals. 11 (2021). https://doi.org/10.3390/cryst11040445.

[62] N.Terao, Structure of tantalum nitrides, Jpn. J. Appl. Phys. 10 (1971) 248–259. https://doi.org/10.1143/jjap.10.248.

[63] L.E.Conroy, A.N.Christensen, Preparation and crystal structure of β-Ta_2N, J. Solid State Chem. 20 (1977) 205–207. https://doi.org/10.1016/0022-4596(77)90069-X.

[64] A.C.Lang, D.S.Katzer, N.Nepal, D.J.Meyer, R.M.Stroud, Phase identification and ordered vacancy imaging in epitaxial metallic Ta_2N thin films, ACS Appl. Mater. Interfaces. 13 (2021) 12575–12580. https://doi.org/10.1021/acsami.0c22244.

[65] H.Li, Z.Cui, Z.Li, S.Zhu, X.Yang, Effect of gas nitriding treatment on cavitation erosion behavior of commercially pure Ti and Ti–6Al–4V alloy, Surf. Coatings Technol. 221 (2013) 29–36. https://doi.org/10.1016/J.SURFCOAT.2013.01.023.

[66] A.K.Niessen, F.R.DeBoer, The enthalpy of formation of solid borides, carbides, nitrides, silicides and phosphides of transition and noble metals, J. Less-Common Met. 82 (1981) 75–80. https://doi.org/10.1016/0022-5088(81)90200-9.

[67] P.C.P.Bouten, A.R.Miedema, On the stable compositions in transition metal-nitrogen phase diagrams, J. Less Common Met. 65 (1979) 217–228. https://doi.org/10.1016/0022-5088(79)90112-7.

[68] F.W.Wood, O.G.Paasche, Dubious details of nitrogen diffusion in nitrided titanium, Thin Solid Films. 40 (1977) 131–137. https://doi.org/10.1016/0040-6090(77)90111-0.

[69] F.L.Yaggee, E.R.Gilbert, J.W.Styles, Thermal expansivities, thermal conductivities, and densities of vanadium, titanium, chromium and some vanadium-base alloys: A comparison with austenitic stainless steel, J. Less Common Met. 19 (1969) 39–51. https://doi.org/10.1016/0022-5088(69)90083-6.

[70] O.N.Senkov, B.C.Chakoumakos, J.J.Jonas, F.H.Froes, Effect of temperature and hydrogen concentration on the lattice parameter of beta titanium, Mater. Res. Bull. 36 (2001) 1431–1440. https://doi.org/10.1016/S0025-5408(01)00604-3.

[71] W.Lengauer, Nitrides: Transition Metal Solid-State Chemistry, in: R.A.Scott (Ed.), Encycl. Inorg. Bioinorg. Chem., John Wiley & Sons Ltd., 2015. https://doi.org/10.1002/9781119951438.eibc0146.pub2.

[72] V.Petukhov, Thermal expansion of zirconium in the solid phase, High Temp. - High Press. 35–6 (2003) 15–23. https://doi.org/10.1068/htjr066.

[73] J.C.Hedge, J.W.Kopec, C.Kostenko, J.L.Lang, Thermal properties of refractory alloys, Chicago, 1963.